Nonthermal Plasma-Modified Carbon-Carrying Sn-Based Ternary Nanocatalyst for High-Performance Direct Dimethyl Ether Fuel Cells

Medhanie Gebremedhin Gebru, Hannan Teller, Palaniappan Subramanian,* and Alex Schechter*

A Vulcan XC72 carbon-supported Sn-based ternary metal catalyst ($Pt_3Pd_3Sn_2$/C) is reported to have yielded the highest specific power density (90 mW mg$^{-1}_{PGM}$) as compared with other catalysts tested for direct dimethyl ether (DME) fuel cells. However, the micropores present in Vulcan XC72 limit fuel utilization by causing Pt agglomeration. Vulcan XC72 composed of nongraphitized carbon species is also prone to corrosion. Therefore, herein, carbon supports such as multiwalled carbon nanotubes (MWCNT), black pearl 2000 (BP2000), and their cold N_2 plasma-treated counterparts are tested to further enhance the activity of the catalyst and systematically describe the comparative advantages over the Vulcan XC-72 carbon. Electroanalytical tests show that $Pt_3Pd_3Sn_2$/BP2000 exhibit excellent performance in terms of electrochemical active surface area, peak current density, and DME oxidation charge. A beneficial effect of plasma activation on the activity is observed only in the case of MWCNT while having no or negative effect on the other carbons. Laboratory fuel cell test indicates that $Pt_3Pd_3Sn_2$ nanoparticles supported on optimized binary carbon support containing 75% plasma-activated MWCNT and 25% BP2000 ($Pt_3Pd_3Sn_2$/75M25B) provides the highest reported power density of 117 mW mg$^{-1}_{PGM}$ at 70 °C fuel cell temperature and ambient pressure.

1. Introduction

Direct dimethyl ether fuel cells (DDMEFCs) are considered to be promising among direct gaseous hydrocarbon-fed low-temperature proton-exchange membrane (LT-PEM) fuel cells for various portable devices.[1–3] The utilization of DME as a fuel in LT-PEM offers several advantages over other hydrogen carrier fuels such as methanol, ethanol, and ammonia due to its high theoretical energy density (8.2 kW h kg^{-1}), low toxicity, ease of storage, and transport in addition to the significantly reduced crossover from the anode to the cathode. So far, DDMEFCs perform best with Pt and Pt-based transition metal catalysts of high activity as cathode and anode active materials, respectively.[4,5] However, the high cost, lack of long-term stability, and Pt metal being readily prone to poisoning by surface-adsorbed fuel oxidation products (CO_{ads}) are the main challenges impeding the further development of DDMEFC technology.

Lowering the loading of Pt-based catalysts and discovering catalysts with improved activities and long-lasting stability are the main features of studies reported thus far in the anode catalyst development research for DDMEFCs.[6,7] One way to increase the catalyst utilization and lower the loading lies in choosing the optimal carbon matrix for supporting the active catalysts. Supporting metal catalysts on suitable solid carbon particles enhances electrocatalytic performance by providing high electrical conductivity, efficient transport of reactants, and effective removal of reaction products along with increased surface area.[8–10] Furthermore, carbon supports can improve catalyst dispersion and hence lower noble metal loading. Various studies have been conducted on chemical and thermal treatments of these supporting materials to alter their surface properties and improve the supported catalyst's electroactivities. Surface modifications of carbons reduce the catalyst agglomeration, increase the electrochemically active catalytic numbers, and further improve the reactant/product transport to and from the catalyst active sites.[11] Among these, low-pressure and nonthermal plasma treatments were shown to induce vacancies/defects that increase the surface energy, porosity, and roughness and introduce reactive heteroatoms (O*, OH*, N, and S) depending on the plasma-generative gas used.[12] Moreover, the nonthermal plasma technique is simple for practical applications and provides high-energy chemical species (electrons, ions, atoms, and molecules) at a low temperature of gases and low cost.[13,14] We have recently studied nonthermal O_2 plasma effects on both single- and multiwalled carbon nanotubes (SWCNT and MWCNT) and reported that an increase

M. G. Gebru, H. Teller, A. Schechter
Department of Chemical Science
Ariel University
Ariel 40700, Israel
E-mail: salex@ariel.ac.il

P. Subramanian, A. Schechter
New Technologies – Research Center
University of West Bohemia
30100 Pilsen, Czech Republic
E-mail: palans@ntc.zcu.cz

The ORCID identification number(s) for the author(s) of this article can be found under https://doi.org/10.1002/ente.202200835.

ADVANCED
SCIENCE NEWS
www.advancedsciencenews.com

Energy Technology
Generation, Conversion, Storage, Distribution

www.entechnol.de

in oxygen heteroatom doping and functional groups on these supports is vital for improving the catalyst performance.[12] Carbon supports with varying inherent properties in terms of porosity, Brunauer–Emmett–Teller (BET) surface area, and conductivity affect the activity of the same catalyst differently. The effect of support surface area on a catalyst activity was studied by Polymeros et al.,[15] using Vulcan XC72R and hollow graphitic spheres (HGS), each containing Pt particles of the same size and loading. They observed a reduced agglomeration and deactivation of the particles in HGS due to their high surface area and porous surface texture. It is also worth highlighting that MnO_2-based oxygen reduction catalysts supported on binary carbons (CNT, BP2000) resulted in enhanced performance both in metal–air battery and microfuel cell.[16] These reports indeed demonstrate that the type and number of carbon support used and their modifications strongly influence the catalytic property of electrodes used in fuel cells.

Vulcan XC72 (XC72) carbon-supported catalyst, $Pt_3Pd_3Sn_2$/C, synthesized in our lab,[17] yielded the highest specific power density (90 mW mg$^{-1}_{PGM}$) compared with other catalysts reported so far in a DDMEFC at low Pt loading and ambient pressure. However, the micropores present in XC72 hinder fuel utilization due to the partial burial of nanoparticles within the carbon layers.[18] Moreover, the sulfur groups present in XC72 could cause sulfur poisoning of nanoparticles.[19] XC72 with higher nongraphitized carbon content is also prone to corrosion.[20] Therefore, utilization of other forms of carbon particles such as Black pearl 2000 (BP2000) and MWCNT as supports is desirable and is likely expected to promote the performance of $Pt_3Pd_3Sn_2$ alloy nanocatalyst. BP2000 has a high BET surface area of 1485 m^2 g^{-1} than XC72 (232 m^2 g^{-1}).[21] MWCNT is known to provide excellent electronic conductivity of >100 S cm^{-1} as compared with XC72 (4 S cm^{-1}).[10,22]

In this study, the effect of N_2 cold plasma treatment of carbon-supporting materials (MWCNT, BP2000, and XC72) on the activity of $Pt_3Pd_3Sn_2$ toward DME electrooxidation was investigated. Comprehensive physicochemical characterization techniques were employed to determine the changes in the structure, morphology, and pore size distribution (PSD) of the carbons and catalyst-coated supports following the nonthermal plasma treatment. The activity of these catalysts was evaluated by conducting electrochemical measurements in a conventional three-electrode cell and a laboratory single-prototype fuel cell. Carbons that yield interesting results were mixed at varying compositions and utilized as supports to harness the desirable properties of each substrate.

2. Results and Discussion

2.1. Physicochemical Characterizations

2.1.1. X-ray Diffractometry

Our previous studies showed that although Sn^{2+} alone cannot undergo a hydrothermal reduction in ethylene glycol, Pt–Sn, and Pd–Sn alloy production by polyol reduction proceeds through the formation of transition metal–tin chloride complexes formed in ethylene glycol during mixing.[17,23,24] These complexes are reduced at an overpotential of 500 mV lower than Sn^{2+}, but higher than Pt or Pd, hence, confirming the formation of Pt–Sn and Pd–Sn alloys.
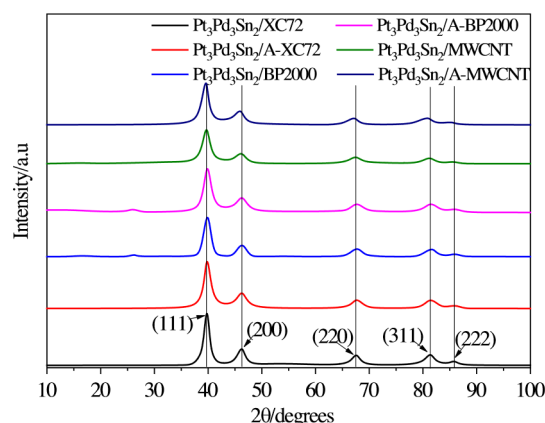

Figure 1. XRD pattern of $Pt_3Pd_3Sn_2$/C catalyst supported on different pristine and plasma-treated carbon supports.

The XRD pattern of $Pt_3Pd_3Sn_2$/C catalyst supported on different pristine and plasma-treated carbon supports is shown in **Figure 1**. The characteristic peaks for catalyst on the different substrates occurred at around 40°, 46°, 67.5°, 82°, and 86° with their corresponding miller indexes (111), (200), (220), (311), and (222), respectively. The peak at around 26° for the catalyst-added pristine and activated MWCNT corresponds to the (022) plane of the graphitized carbon support.[25] The catalyst has a face-centered cubic (FCC) crystal structure with a space group of $Fm\text{-}3m$ (DB Card Number 9 004 088). These patterns are best matched with the Atokite phase from the XRD database that has a chemical formula of $(PtPd)_{1.5}Sn$. Atokite phase peaks are known to appear at 2θ of 39.06°, 45.41°, 66.17°, 79.60°, and 83.92°. Therefore, it is clear that the XRD patterns for the prepared catalyst show a 0.5°–1.5° positive shift, with the shift being highest (>1°) for the BP2000-supported catalyst. The d-spacing obtained using the (220) plane (d_{220}) for $Pt_3Pd_3Sn_2$/BP2000 was 13.8 Å, whereas for both $Pt_3Pd_3Sn_2$/MWCNT and $Pt_3Pd_3Sn_2$/XC72 it was 14.2 Å. According to Bragg's law, the decrease in the distance between the planes for $Pt_3Pd_3Sn_2$/BP2000 is the cause for its relatively larger X-ray peak shift.[26] A slight variation in the lattice unit cell size was observed among the prepared catalysts with the value ranging from 3.91 Å for $Pt_3Pd_3Sn_2$/BP2000 to 4.03 Å for $Pt_3Pd_3Sn_2$/MWCNT. The compressed lattice unit cell of the particles on BP2000 is an indication of the particles' confinement in the micropores of the support, as discussed in the later sections. The large surface area of the porous support also provides more contact points that strengthen the interactions at the $Pt_3Pd_3Sn_2$ alloy-BP2000 interface and hence, could contract the planes.[27] There was a 0.06 Å decrease in the d_{220} of the BP2000-supported catalysts following the plasma activation of the carbon. However, due to the more graphitic nature of MWCNT and XC72, plasma activation of these supports did not lead to a similar effect on the d_{220} spacing value of the catalyst.

The average particle crystallite size was calculated using Scherer's equation from the peak indexed to the plane (220). Accordingly, the metal particles in $Pt_3Pd_3Sn_2$/BP2000 had the smallest crystallite size of 3.69 nm in line with the better dispersion of the metallic particles. In contrast, the largest ones are present in the $Pt_3Pd_3Sn_2$/MWCNT (5.70 nm) followed by

ADVANCED
SCIENCE NEWS
www.advancedsciencenews.com

Energy Technology
Generation, Conversion, Storage, Distribution
www.entechnol.de

Table 1. Elemental analysis of $Pt_3Pd_3Sn_2$ on plasma-activated nonactivated carbon supports.

Catalyst	Precursor atomic ratio	ICP-OES atomic ratio	EDS atomic ratio
$Pt_3Pd_3Sn_2$-XC72	1.5:1.5:1	1.43:1.47:1	1.45:1.47:1
$Pt_3Pd_3Sn_2$-A-XC72	1.5:1.5:1	1.46:1.45:1	1.44:1.47:1
$Pt_3Pd_3Sn_2$-MWCNT	1.5:1.5:1	1.44:1.46:1	1.47:1.45:1
$Pt_3Pd_3Sn_2$-A-MWCNT	1.5:1.5:1	1.43:1.48:1	1.45:1.41:1
$Pt_3Pd_3Sn_2$-BP2000	1.5:1.5:1	1.46:1.47:1	1.50:1.44:1
$Pt_3Pd_3Sn_2$-A-BP2000	1.5:1.5:1	1.47:1.50:1	1.48:1.48:1

$Pt_3Pd_3Sn_2$/XC72 (4.18 nm). The particle crystallite size showed a decrease by 0.2–0.6 nm following the plasma activation of MWCNT and BP2000, respectively, which could be due to the confinement of particles into micropores and defects introduced during the nonthermal plasma treatment step. The ICP–OES and EDS elemental analysis show that the metal content and atomic ratios were very close to the expected nominal values, which shows the assay of the obtained product (**Table 1**). Moreover, the measured atomic ratios are nearly the same regardless of the type of carbon support and treatment. This confirms that the changes in the lattice parameters are caused by the support–metal interactions at the interface rather than the variation of the alloy composition. The metal composition of the prepared carbon-supported catalyst was 66–71% showing no considerable difference from the intended percentage, 70%.

2.1.2. Raman Spectroscopy

The Raman spectra of the pristine supports are shown in **Figure 2**a. Two peaks appeared at around 1350 and 1580 cm^{-1} corresponding to the D and G-bands. The D-band is attributed to the A_{1g} mode vibration of the sp^3-hybridized graphitic carbon atoms[28] and the G-band is ascribed to the E_{2g} mode vibration of the sp^2-hybridized carbon atoms in the 2D hexagonal rings.[29] The degree of graphitization and defects present (maximum intensity ratio at D- and G-bands (I_D/I_G)) of the XC72, BP2000, and MWCNT were 1.10, 1.28, and 0.98, indicating that BP2000 followed by XC72 has a lower degree of graphitization (sp^2 graphitic nature). MWCNT has the most intense D band attributed to the presence of a higher number of naturally occurring ring defects.

Figure 2b shows the Raman spectra of the N_2 plasma-activated carbons. The plasma treatment caused a 17% increase in the I_D/I_G ratio for MWCNTs relative to its pristine counterpart. This is attributed to the formation of more chemical defects. However, in the case of XC72 and BP2000, this ratio showed a slight decrease (4.5% and 2.3%, respectively) suggesting the removal of the surface layers or functional groups from these softer black carbons by plasma etching.[30]

2.1.3. Fourier-Transform Infrared Spectroscopy and CHNS/O

Shown in Figure 2c is the FTIR spectra of the different pristine carbon supports. Bands in the region of 3100–3700 and 2890–2900 cm^{-1} corresponding to O–H/N–H stretching and aliphatic groups, respectively, are similar in all the carbon samples.[31] C=O (carboxylic acid, ketone/quinone) and C=C (aromatic rings) groups can be observed at 1700 and 1630 cm^{-1}, respectively.[32] The peaks at 1270–1000 cm^{-1} are assigned to C—O, and C—O—C bonds.[32] Most of the FTIR fingerprints of the MWCNT spectrum are also seen in XC72 (Figure 2c). Relative to XC72, pristine MWCNT possesses additional peaks at 1180 and 910 cm^{-1}, corresponding to C—O and C–H stretching.[28] In general, BP2000 has fewer characteristic
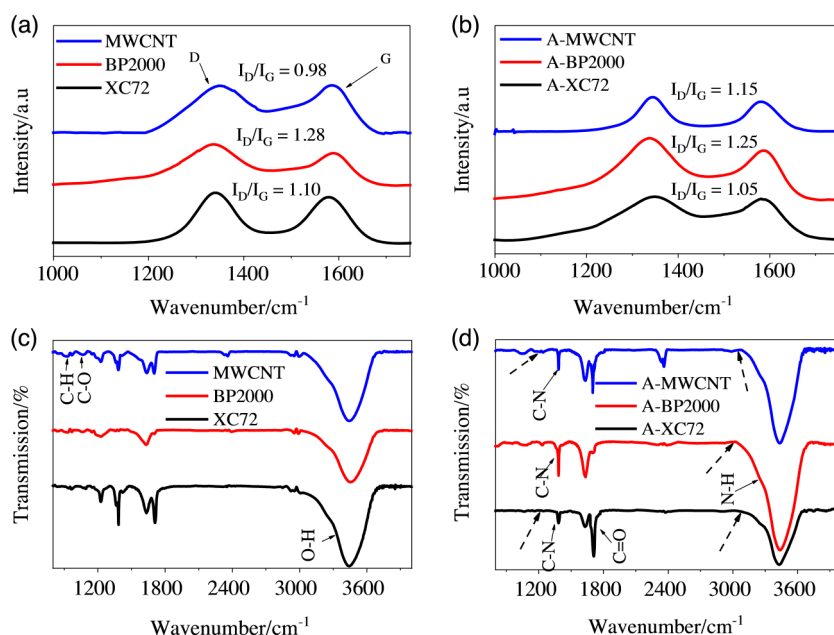

Figure 2. a,b) Raman and c,d) FTIR spectra of pristine ((a) and (c)) and N_2 plasma-activated ((b) and (d)) BP2000, MWCNT, and XC72 carbon supports.

functional groups than MWCNT and Vulcan XC72, which can easily be observed from the missing bands of C–H bending and C=O stretching at 1380 and 1710 cm^{-1}, respectively.

The FTIR spectra of the carbons exposed to the 5 min N$_2$ plasma treatment are displayed in Figure 2d. The additional sharp peak at 1380 cm^{-1} (for all the carbons) and the increase in the intensity of the peak at 3100–3700 cm^{-1} (for MWCNT and BP2000) indicate that the plasma treatment introduced new C–N and N–H (pyrrolic N) functional groups, respectively. This shows the successful doping of the nitrogen atoms. The minor peak at around 1150 cm^{-1} indicates that trace amounts of the C–N group are already present in the pristine MWCNT and XC72.[33] Even though the plasma treatment was under an N$_2$ environment, the intensification of the peak at 1710 cm^{-1} (for all the carbons) that corresponds to the C=O bond suggests the incorporation of O atoms. As described by Subramanian et al.,[34] the inclusion of O atoms occurred during exposure of the broken carbon bonds to air when taking the sample out of the plasma chamber. CHNS/O analysis (Table S1, Supporting Information) further confirms nitrogen doping as wt% of nitrogen for A-XC72, A-BP2000, and A-MWCNT increases by 12.68%, 8.49%, and 10.26%, respectively, relative to their pristine counterparts. An increase in the wt% of oxygen was also observed for all these carbons after the treatment. Nonetheless, plasma activation has also resulted in the removal of functional groups. The intensity of the FTIR spectra at 920, 1230, and 2850–3000 cm^{-1} corresponding to C–H bending, C–O stretching, and C–H stretching, respectively, has significantly decreased/disappeared for all the carbon supports after the treatment (dashed black arrows). As some of these spectra are not fully diminished, it can be concluded that the plasma treatment only removed the weakly bonded surface functional groups mainly due to etching rather than from the bulk.

2.1.4. Scanning Transmission Electron Microscopy

The STEM images of Pt$_3$Pd$_3$Sn$_2$ supported on pristine and N$_2$ plasma-activated XC72, BP2000, and MWCNT are presented in **Figure 3**a–f. Before activating the carbons, despite the high metal loading of the catalysts in our preparation method, uniform and better dispersion of the particles was observed on BP2000 and MWCNT. Some local particle agglomerations are still seen, especially on MWCNT. However, in the case of XC72, the particles are highly aggregated in line with previous observations.[19] Better particle scattering observed on BP2000 is attributed to the exceptionally high BET surface area of the support (Table S2, Supporting Information).

After N$_2$ plasma treatment, MWCNT showed the most significant improvement in the particle distribution relative to the other carbons (Figure 3e,f, S5a,b, Supporting Information) consistent with its highest increase in the defects relative to the other carbons (17% increase in the I_D/I_G ratio). In contrast, the treatment exacerbated particle dispersion on both BP2000 and XC72 (Figure 3a–d). This is ascribed to the smoothening of the surface layers evidenced by the slight decrease in the I_D/I_G ratio (Figure 2a) and hosting of more metal particles in the newly introduced pores, as explained in the next section. The size distribution of the nanoparticles supported on the pristine and

plasma-activated carbon supports was calculated by measuring the diameter of 50 randomly picked nanoparticles from Figure 3 and is displayed in a histogram in Figure S1, Supporting Information.

2.1.5. BET Surface Area and Pore Size Analysis

The PSD and N$_2$ adsorption/desorption isotherms of the pristine and plasma-treated supports are displayed in **Figure 4**a–f. The change in the isotherm of the pristine carbons upon the addition of the metal catalysts is also shown in the same figure and a similar conclusion can be drawn for the treated ones. The BET surface area and PSD of the carbon supports are summarized in Table S2, Supporting Information. The N$_2$ adsorption/desorption of all the samples exhibit a hysteresis loop of type IV isotherm indicating the presence of mesopores and macropores.[35] The loop is formed as the dependence of the capillary condensation and evaporation processes of the N$_2$ molecules during its adsorption and desorption, respectively, on the pressure is different.[36] The average pore diameter of the black carbons (XC72 and BP2000) significantly increased after N$_2$ plasma treatment is ascribed to the formation of new pores and breakage of walls between adjacent pores to form larger ones. This is consistent with the previous observation by Mohan et al.[37] who reported that cold plasma pretreatment of BP2000 formed small void spaces and increased the pore volume of the support. The effect of the plasma treatment on the change in the pore diameter of the MWCNT pores was minimum relative to the black carbons.

When the catalyst is incorporated into the carbons during the synthesis, the adsorption/desorption isotherm (the N$_2$ uptake) of XC72 and BP2000 has been reduced significantly which clearly shows that the metal particles were hosted inside the pores (Figure 4b,f). However, in the case of MWCNT, the N$_2$ uptake is nearly unchanged by the metal incorporation indicating deposition of the metals on sidewalls of the inner and outer surface of the tubes rather than being hidden within the pores present on the surfaces. As was reported by Tong et al.,[38] the surface functional groups of MWCNT favor the dispersion of metal nanoparticles on the surface by providing sufficient-anchoring sites. Our FTIR analysis revealed that MWCNT has more surface functional groups as compared with BP2000 and XC72. This, regardless of its lowest BET surface area (173 m^2 g^{-1}), enabled MWCNT to attach the particles to the inner and outer surfaces of the tubes and improve their fuel/electrolyte accessibility.

2.2. Electrochemical Measurements

Figure 5a,b shows the effect of pristine and plasma-treated carbon supports on Pt$_3$Pd$_3$Sn$_2$ activity toward DME oxidation and the results are summarized in **Table 2**. The ECSA of Pt$_3$Pd$_3$Sn$_2$/BP2000 (9.74 ± 0.06 m^2 g^{-1}$_{PGM}$) and Pt$_3$Pd$_3$Sn$_2$/A-XC72 (6.32 ± 0.12 m^2 g^{-1}$_{PGM}$) were the highest and lowest, respectively. The ECSA was calculated from the average charge (Q_A) obtained in the hydrogen adsorption–desorption region (H_{UPD}) (0–0.35 V) of the cyclic voltammogram (CV) recorded in an N$_2$-saturated 0.5 M H$_2$SO$_4$ (Figure 5c,d) using Equation (1).[39]
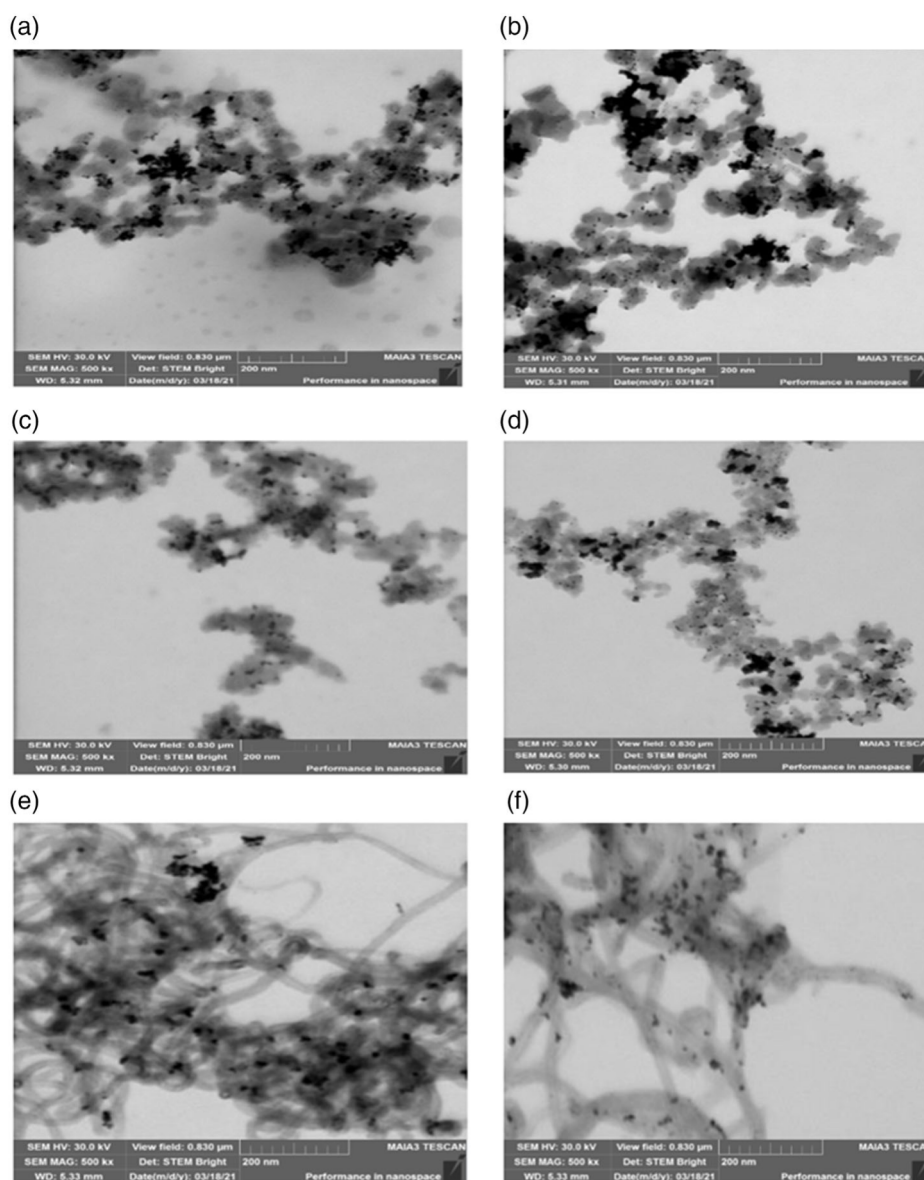
**ADVANCED
SCIENCE NEWS**

www.advancedsciencenews.com

Energy Technology
Generation, Conversion, Storage, Distribution

www.entechnol.de

Figure 3. a,c,e) STEM image of $Pt_3Pt_3Sn_2$ supported on pristine and b,d,f) N_2 plasma-activated XC72, BP2000, and MWCNT, respectively.

$$ECSA = \frac{Q_A}{Q_H L_{PGM}} \qquad (1)$$

where Q_H is the columbic charge required to remove a single layer of adsorbed hydrogen atoms per unit area, usually taken as $2.1 \times 10^{-5}\,mC\,m^{-2}$, and L_{PGM} is the platinum group metal (PGM) content present in the catalyst.

Considering the highest BET surface area of BP2000, the ECSA obtained with $Pt_3Pd_3Sn_2$/BP2000 was not significantly higher than on pristine and activated MWCNT. This is attributed to the insertion of the catalyst particles within the pores of the black carbons, making them inaccessible to the electrolyte. The region between 0.35 and 0.6 V is the double-layer region formed by the array of charged species at the electrode–solution interface. In the N_2-saturated solution, the Pt and/or Pd oxides

that started to be formed at around 0.9 V during the positive scan are reduced during the reverse scan, showing a cathodic peak at about 0.8 V. With the same metals and loadings used in all the catalysts, the obvious difference in the H_{UPD} and the Pt/Pd oxide formation/reduction regions among the catalysts signifies the effect of carbon supports and their plasma activation on the ECSA and catalyst activity.

In a DME-saturated solution, the H_{UPD} region is suppressed due to the competitive adsorption of DME and hydrogen on the same active sites.[40] For all the catalysts, the non-faradaic double-layer current of the CV recorded in a DME-saturated solution decreased relative to the N_2-saturated solution. This is attributed to the anodic current yield due to the oxidation of the DME molecules adsorbed during the reverse scan between 0.8 and 0.7 V. In the anodic potential scan, DME oxidation begins
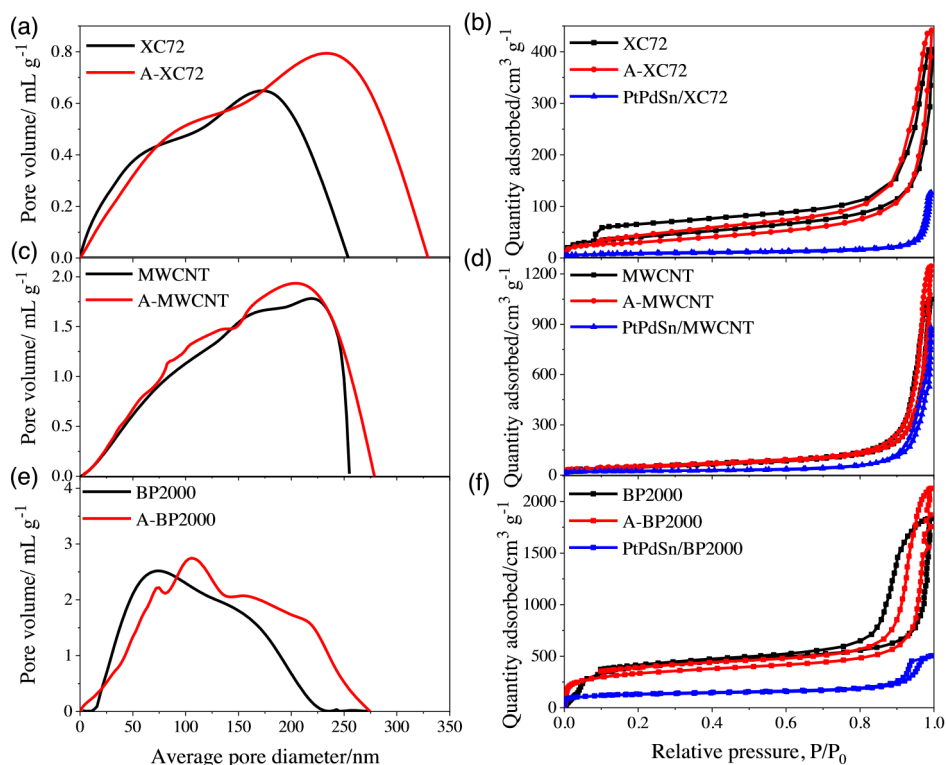
**ADVANCED
SCIENCE NEWS**

www.advancedsciencenews.com

Energy Technology
Generation, Conversion, Storage, Distribution

www.entechnol.de

Figure 4. a,c,e) PSD and b,d,f) N_2 adsorption/desorption isotherms of the pristine and N_2 plasma-activated carbon supports.
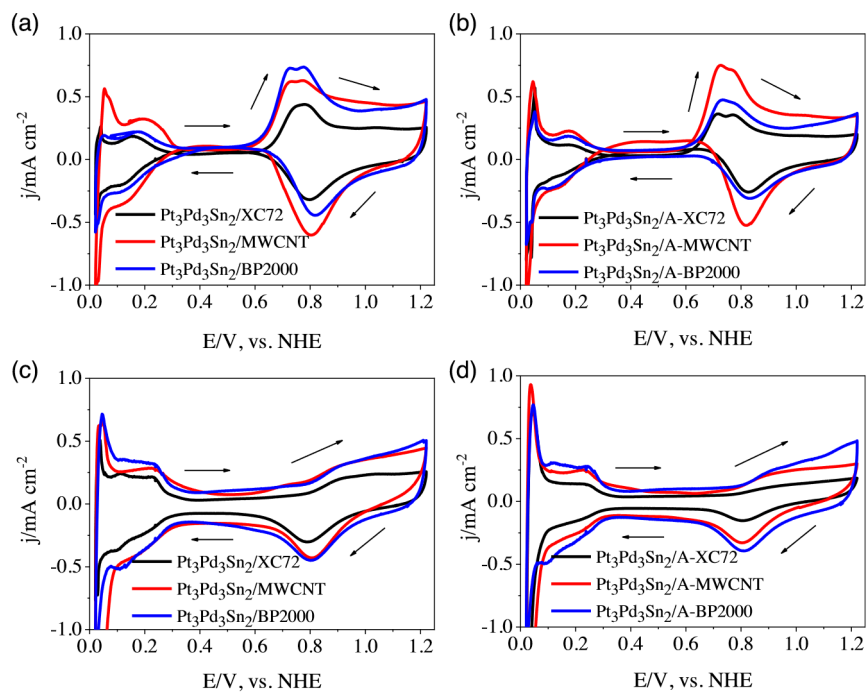

Figure 5. CV for $Pt_3Pd_3Sn_2$ supported on a,c) pristine and cold b,d) plasma-treated carbon supports in DME (a,b) and N_2 (c,d) saturated solutions (0.5 M H_2SO_4 electrolyte, 10 mV s^{-1} scan rate, and 100 µg cm^{-2} catalyst loading).

Table 2. Electrochemical parameters of Pt$_3$Pd$_3$Sn$_2$ on different carbon supports.

Catalysts / Parameters	ECSA [m^2]	j_p [mA cm^{-2}]	E_p [V, vs. NHE]	Q_{oxi} [mC]	Onset potential [E, vs. NHE]
Pt$_3$Pd$_3$Sn$_2$/XC72	6.88 ± 0.18	0.45 ± 0.02	0.77 ± 0.01	163 ± 2.14	0.58 ± 0.03
Pt$_3$Pd$_3$Sn$_2$/A-XC72	6.32 ± 0.12	0.36 ± 0.01	0.72 ± 0.03	138 ± 1.46	0.55 ± 0.01
Pt$_3$Pd$_3$Sn$_2$/MWCNT	9.22 ± 0.12	0.64 ± 0.02	0.77 ± 0.02	287 ± 2.83	0.52 ± 0.00
Pt$_3$Pd$_3$Sn$_2$/A-MWCNT	9.35 ± 0.06	0.67 ± 0.02	0.72 ± 0.02	303 ± 4.24	0.51 ± 0.01
Pt$_3$Pd$_3$Sn$_2$/BP2000	9.74 ± 0.08	0.74 ± 0.00	0.78 ± 0.00	309 ± 13.70	0.53 ± 0.00
Pt$_3$Pd$_3$Sn$_2$/A-BP2000	8.14 ± 0.24	0.46 ± 0.01	0.73 ± 0.03	174 ± 3.46	0.53 ± 0.03
Pt$_3$Pd$_3$Sn$_2$/25M75B	12.94 ± 0.43	0.67 ± 0.09	0.74 ± 0.00	255 ± 10.97	0.51 ± 0.00
Pt$_3$Pd$_3$Sn$_2$/50M50B	14.59 ± 0.55	0.72 ± 0.06	0.73 ± 0.00	295 ± 21.21	0.51 ± 0.00
Pt$_3$Pd$_3$Sn$_2$/75M25B	19.13 ± 1.34	1.01 ± 0.06	0.72 ± 0.00	395 ± 21.92	0.51 ± 0.00

at around 0.50–0.58 V, depicting two peaks in the range of 0.72–0.78 V. Earlier reports on DME electro-oxidation on Pt-based catalysts ascribed these two peaks to the sequential oxidation of CO$_{ads}$ and CHO$_{ads}$.[41] Beyond 0.8 V, the formation of surface oxides leads to the rapid decline of the curves.[40] During the reverse scan, the highest anodic current was obtained by Pt$_3$Pd$_3$Sn$_2$/A-MWCNT. This is attributed to the introduction of defects by the plasma treatment that formed more catalyst deposition sites on the support, resulting in an increased number of DME oxidation sites. In addition, the nitrogen modification (N–H or C–N functional groups) on the A-MWCNT may have introduced some improvement effect on the MWCNT supports by improving the attachment of the catalyst particles or the electronic conductivity.

Pt$_3$Pd$_3$Sn$_2$/BP2000 gave the highest DME oxidation charge (Q_{oxi}) of 309 mC which is only marginally higher than Pt$_3$Pd$_3$Sn$_2$/A-MWCNT (303 mC) but significantly higher than Pt$_3$Pd$_3$Sn$_2$/A-XC72 (167 mC). Q_{oxi} was calculated by integrating the currents under the DME oxidation peak region of the CV at around 0.6–1 V (Figure 5a,b). Moreover, Pt$_3$Pd$_3$Sn$_2$/BP2000 provided the maximum peak current density (j_p) as 0.74 mA cm^{-2}. Even though the BET surface area of BP2000 was about 8 times higher than that of A-MWCNT, Pt$_3$Pd$_3$Sn$_2$/A-MWCNT gave a comparable j_p and Q_{oxi} as Pt$_3$Pd$_3$Sn$_2$/BP2000. The spectral

analysis (FTIR and Raman) showed that A-MWCNT has excess functional groups (C–H and C–O) and a higher number of defects (Figure 2a,c). This facilitated metal particle deposition on the sidewalls of the tubes and increased the dispersion sites, respectively, by improving the particle accessibility to DME. The improved conductivity of A-MWCNT also enhances the reaction kinetics by weakening the PtPdSn–CO bond strength. An oxidative stripping of a monolayer preadsorbed CO (CO$_{ads}$) using Pt$_3$Pd$_3$Sn$_2$ supported on different carbons was conducted to confirm this. As shown in **Figure 6**a, the A-MWCNT-supported catalyst showed a 25 and 90 mV lower CO$_{ads}$ oxidation onset and peak potentials relative to Pt$_3$Pd$_3$Sn$_2$/BP2000. Therefore, the 20–50 mV lower DME oxidation onset potential exhibited by Pt$_3$Pd$_3$Sn$_2$/A-MWCNT as compared with other supports is attributed to the better removal of intermediates such as CO$_{ads}$ by this catalyst.

Except for the MWCNT, which improved catalyst activity when activated, the plasma treatment of the other carbon supports had a negative effect. In the case of XC72 and BP2000, the N$_2$ plasma treatment resulted in the formation of additional pores that confined the metal particles, hence, reducing their utilization. This, in addition to the pore size analysis discussed earlier (Figure 4), was confirmed from a CV recorded in an N$_2$-saturated 0.5 M of H$_2$SO$_4$ solution using a working electrode loaded with just the
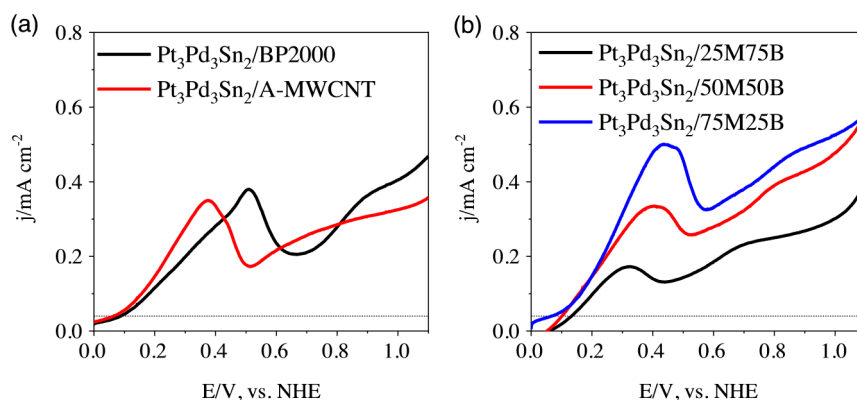

Figure 6. Oxidative stripping (LSV) of CO$_{ads}$ for catalyst supported on a) single and b) mixture of carbon materials (catalyst loading 50 µg cm^{-2}, scan rate 5 mV s^{-1}, electrolyte 0.5 M H$_2$SO$_4$).

ADVANCED
SCIENCE NEWS
www.advancedsciencenews.com

Energy Technology
Generation, Conversion, Storage, Distribution
www.entechnol.de

pristine and plasma-treated carbon supports (Figure S2, Supporting Information). The increase in the currents at the double-layer region for the plasma-activated black carbons shows an increase in the surface area due to the formation of additional pores. Despite the plasma-induced improvements on the MWCNT, the electrochemical properties (ECSA, j_p, and Q_{oxi}) of $Pt_3Pd_3Sn_2$/BP2000 were still the highest, attributed to the large initial surface area of the support.

2.3. Combination of Carbon Supports

To harness the properties of each of the catalyst substrates, namely, the high surface area and dispersion provided by BP2000 and the high conductivity and functional groups (anchoring sites) from the MWCNT, mixtures of these carbons were studied as $Pt_3Pd_3Sn_2$ supports while maintaining the same metal loading (70%) as for the single carbons. As the positive effect of plasma treatment was only observed in the case of MWCNT, pristine BP2000 and N_2 plasma-activated MWCNT were combined at different wt% ratios. LSV measured with the catalyst supported on carbon mixtures was compared to the single carbon-supported catalyst, as shown in **Figure 7**a. The difference in the activity of the catalyst when the two supports are mixed during the synthesis was compared with postsynthesis mixing of two separately prepared catalysts and no significant difference was witnessed (Figure S3, Supporting Information).

In general, it is observed that with an increase in the A-MWCNT content in the mixture, the j_p and Q_{oxi} also increased and peaked at an MWCNT content of 75% (Table 2). The catalyst supported on a mixture of 75% of plasma-activated MWCNT and 25% pristine BP2000 (labeled as $Pt_3Pd_3Sn_2$/75M25B) gave a j_p of 1.01 ± 0.06 mA cm^{-2} and Q_{oxi} of 395 mC mg$^{-1}_{PGM}$ which is around 27% and 22%, respectively, enhancement relative to BP2000-supported $Pt_3Pd_3Sn_2$.

While dispersing 75% MWCNT and 25% BP2000 (wt%) together in ethylene glycol, the BP2000 might have been inserted into the MWCNT tubes, enabling the particles to be supported on
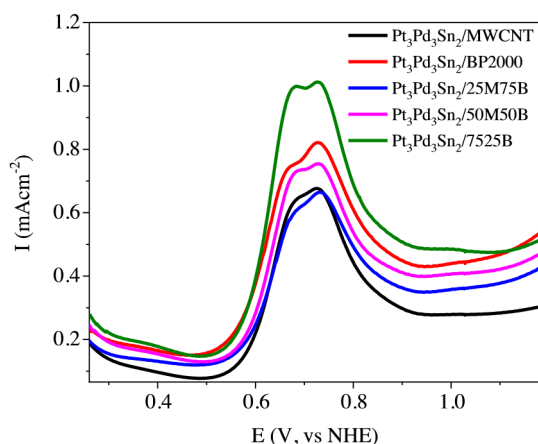
the outer surface of the tubes. This improves the exposure of the particles to the electrolyte/DME fuel. A STEM image of the particles supported on BP2000, 25M75B, and 75M25B is included in Figure S4, Supporting Information. With the same magnification for all the samples, the particles supported on the 75M25B are more visible. Moreover, the BP2000 component of 75M25B is not observed, confirming its incorporation into the tubes. The Q_{oxi} and j_p of $Pt_3Pd_3Sn_2$ supported on the carbon mixture with higher BP2000 content (25M75B and 50M50B) were lower than the values attained by $Pt_3Pd_3Sn_2$/BP2000. BP2000 in these carbon mixtures is therefore not only acts as a tube filler but also covering the outer tube surfaces. As shown in Figure S4c, Supporting Information, the majority of the particles are rather supported on the BP2000 component of the mixture. This reduces MWCNT-PtPdSn contact and hence, the electronic role of MWCNT. This was confirmed from the electrochemical stripping of preadsorbed CO on $Pt_3Pd_3Sn_2$ supported on 25M75B, 50M50B, and 75M25B mixed-carbon materials, as shown in Figure 6b. The CO_{ads} oxidation onset potential of $Pt_3Pd_3Sn_2$ on 75M25B (70 mV) was lower than the support mixture with higher BP2000 contents. The highest j_p of CO_{ads} oxidation obtained with 75M25B as compared with the single carbons indicates the presence of more number of oxidation active sites, which is reflected by its highest ECSA.[42]

Chronoamperometry was recorded for 90 min with $Pt_3Pd_3Sn_2$ supported on MWCNT, A-MWCNT, BP2000, and 75M25B at 0.6 V in a DME-saturated 0.5 M H_2SO_4 solution to study the effect of treatment and carbon mixing on the catalyst stability (**Figure 8**). In all the catalysts, the current decays fast in the first few seconds ($<\approx$100 s) due to the fast movement of ions toward the electrode surface to complete the double-layer (capacitive) charging. Beyond this time, a steady-state faradaic current begins to be produced from the oxidation of DME on the electrode surface. $Pt_3Pd_3Sn_2$/MWCNT appeared to have the lowest stability as the oxidation proceeded. However, the catalyst supported on BP2000 and A-MWCNT showed stable current density throughout the oxidation duration. The strong metal–support interaction that arises from the larger metal–support contact area (in the case of BP2000) and the plasma-induced defects and functional groups (in the case of A-MWCNT) contributed to this stability. $Pt_3Pd_3Sn_2$/75M25B also provided a stable and active catalyst
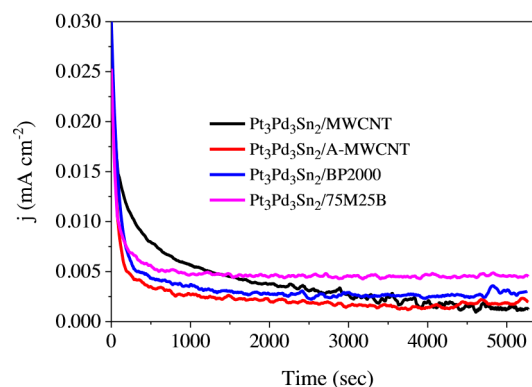

Figure 7. a) LSV of $Pt_3Pd_3Sn_2$ on a single and mixture of BP2000 and MWCNT (0.5 M H_2SO_4 electrolyte, 10 mV s^{-1} scan rate, and 100 µg cm^{-2} catalyst loading).

Figure 8. Constant potential (0.6 V) stability test of the catalysts in a DME-saturated 0.5 M H_2SO_4 with 100 µg cm^{-2} catalyst loading.

**ADVANCED
SCIENCE NEWS**

www.advancedsciencenews.com

Energy Technology
Generation, Conversion, Storage, Distribution

www.entechnol.de

which could be due to the cooperative effect of these two supports in this optimized mixture.

In addition to the previously given explanations, we believe that a detailed understanding of the origins of the improved DME kinetics with the selected support mixture is necessary. For this, comprehensive characterizations of the carbon mixtures and electrochemical impedance spectroscopy measurements using carbon mixture-supported catalysts are underway and will be published in the future.

2.4. Fuel Cell Measurements

The polarization curves of DDMEFC with anode catalyst $Pt_3Pd_3Sn_2/C$ supported on MWCNT, BP2000, and 75M25B carbon materials are displayed in **Figure 9**. A maximum power density of $181\ mW\ cm^{-2}$ was measured with fuel cells containing 1.55 and $2.2\ cm^{-2}$ of $Pt_3Pd_3Sn_2/75M25B$ and Pt black at the anode and cathode was observed at 0.5 V, respectively. This is around 15% and 24% higher than fuel cells with the same anode loading on BP2000 and MWCNT as sole carbon support, respectively (at 0.43 V). This observation is in line with the results obtained in the three-electrode cell presented in the previous sections and further supports the combined support effect of the surface area and conductivity giving $Pt_3Pd_3Sn_2$ a better activity toward DME electro-oxidation.

The corresponding E_{OC} values of DME/Air with $Pt_3Pd_3Sn_2/$ 75M25B, $Pt_3Pd_3Sn_2/BP2000$, and $Pt_3Pd_3Sn_2/MWCNT$ were 910, 874, and 830 mV. Santasalo-Aarnio et al.[43] reported that operating temperature, fuel crossover, type of catalyst, and electrode surface morphology parameters affect the E_{OC}. We assigned the variation in the E_{OC} among the catalysts on different supports to the variation in their catalyst utilization and charge transfer resistance influenced by the support materials composition. The lowest activation losses of $Pt_3Pd_3Sn_2/75M25B$ are related to the optimization of the high conductivity and surface area of the support mixture in enhancing the mass transport and catalyst utilization.

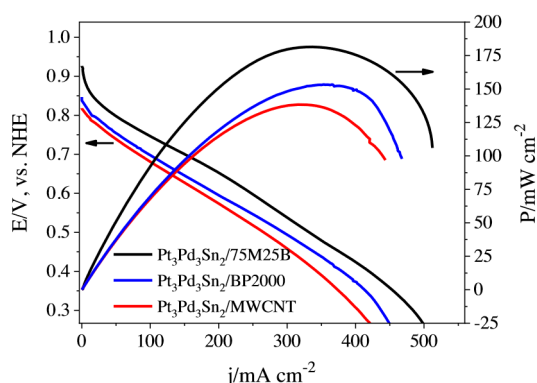It is important to mention that considering the catalyst loading and fuel cell operating temperature used in this study, the acquired power density ranks this catalyst as the best catalyst reported so far for the DDMEFC applications. Table S3, Supporting Information, compares the loading, gas flow rate, fuel cell temperature, and the power output of previously reported catalysts for DDMEFC with our catalyst. This optimized carbon composition stresses the importance of support optimization in terms of conductivity and surface area (dispersion). Thus, the BP2000 lower conductivity is balanced by the MWCNT at an MWCNT-to-BP2000 ratio of 3:1.

3. Conclusion

Nonthermal plasma was successfully used to modify different carbons (BP2000, MWCNT) carrying $Pt_3Pd_3Sn_2$ nanocatalyst. The electrochemical performance of these plasma-modified carbon carriers for catalytic nanoparticles was compared with the unmodified carbon support (XC72). Catalyst supported on BP2000 showed the highest peak current density (j_p) and DME oxidation charge (Q_{oxi}) among all studied pristine carbon materials. This is due to the strong metal–support interaction, higher pore volume, and surface area of the support, resulting in the formation of smaller and more dispersed catalyst nanoparticles. When the carbons were activated, the catalyst activity improvement was observed only in the case of MWCNT. Plasma activation introduced additional defects and functional groups in MWCNT. $Pt_3Pd_3Sn_2/A$-MWCNT offered the most desirable electrochemical properties relative to $Pt_3Pd_3Sn_2/$ BP2000 due to the higher defects and functional groups introduced during nonthermal plasma treatment. Binary carbon supports composed of 75% of plasma-activated MWCNT and 25% BP2000 exhibited 30% higher power output than $Pt_3Pd_3Sn_2$ on unmodified XC72 in a gas-fed low-temperature direct DME fuel cell.

4. Experimental Section

Materials: BP2000, MWCNT, and XC72 were purchased from CABOT Corporation, Sigma Aldrich, and FuelCellStore, respectively. DME, LiCl, and $SnCl_2$ were acquired from Sigma Aldrich. K_2PtCl_4 and $PdCl_2$ were obtained from STERM chemicals. NaOH and H_2SO_4 were purchased from MERCK and CARLO ERBA reagents, respectively. Throughout the experiments, distilled water of $18.2\ M\Omega$ resistance was utilized.

Synthesis of $Pt_3Pd_3Sn_2/C$ Catalyst: The metal precursors, K_2PtCl_4, $PdCl_2$, and $SnCl_2$ were initially dissolved in ethylene glycol separately and mixed. The dissolution of K_2PtCl_4 and $PdCl_2$ was facilitated by adding 0.01 M of LiCl.[44] The pH of the solution was adjusted to 12 by adding 4 M NaOH (in ethylene glycol). The precursor solution was then mixed with either the pristine (XC72, BP2000, and MWCNT) or N_2 plasma-activated (A-XC72, A-BP2000, and A-MWCNT) substrates which were dispersed in ethylene glycol. The metal-to-carbon weight ratio was maintained at 0.7. This solution was refluxed at 180°C for 2 h and then stirred for 12 h at 25 °C. The resulting dispersion was washed with a mixture of distilled water and acetone (3:1, V:V) several times.

Plasma activation of the supports was performed in a low-pressure plasma cleaner (Zepto, Diener Electronic GmbH, Ebhausen), following the procedure described in the literature.[12] A required amount of carbon was inserted into the plasma chamber using a glass Petri dish, and evacuation was performed until the pressure inside was slowly reduced to 0.01 mbar. Then, the plasma chamber pressurized with N_2 gas up to 1.2 mbar plasma was generated for 5 min at 100 W. During the treatment, a very small amount of carbon sample was well spread in a large-diameter

Figure 9. DME fuel cell steady-state polarization curve and power profile at a potential scan rate of $5\ mV\ s^{-1}$. The anode and cathode PGM loading of 1.55 and $2.2\ mg_{PGM}\ cm^{-2}$, respectively. 100% humidified anode (DME) and cathode (air) reactants at flow rates of 30 and $400\ mL\ min^{-1}$, respectively. Fuel cell temperature of 70 °C and ambient pressure.

Petri dish forming a thin layer to ensure that most of the sample was exposed to the ionized nitrogen. A $Pt_3Pd_3Sn_2$ supported on a combination of two of the best-performing carbons mixed at varying compositions was also prepared by the same method and metal-to-carbon weight ratio as above. The electrochemical response of $Pt_3Pd_3Sn_2$ supported on these mixtures was compared with single carbons.

Physicochemical Characterization: The atomic ratios of the metals (Pt, Pd, and Sn) in the prepared catalysts were analyzed using energy-dispersive X-ray spectroscopy (EDS) (AZtec, Oxford instruments) and inductively coupled plasma–optical emission spectrometry (ICP-OES) (Varian ICP-OES 720).

The crystal structures of the catalysts and phases present were determined using X-ray diffraction (XRD) (SmartLab, Rigaku). A scanning transmission electron microscope (STEM) (Tescan MAIA3 Triglav, Brno-Kohoutovice) was employed to study the microstructure of the synthesized catalysts. The functional groups and defects present in the pristine and N_2 plasma-treated carbon supports were analyzed with Fourier-transform infrared spectroscopy (FTIR) (VERTEX 70, Bruker) and Raman spectroscopy (XploRa, HORIBA Scientific), respectively. CHNS/O elemental analysis was performed on all the carbons using an elemental analyzer (FlashSmart, Thermo Scientific) to determine the content of heteroatoms before and after the plasma treatment.

Determination of the surface area and PSD was performed using surface area and porosimetry analyzer (V-Sorb 2800P, APP gold instruments). The surface area was calculated by the BET method in the P/P_o range of 0.06–0.25. Barrett–Joyner–Halenda's model from the N_2 adsorption data was used to calculate the PSD.

Electrochemical Analysis: The electrochemical measurements were controlled by a potentiostat (VSP, BioLogic) at room temperature. The performance of each catalyst was evaluated in a three-electrode system using Pt mesh and Ag/AgCl as counter and reference electrodes, respectively. All the potentials are expressed versus the normal hydrogen electrode (NHE) unless specifically mentioned otherwise. The working electrode was prepared by drop casting a 5 µL catalyst ink on a 0.196 cm^2 glassy carbon (GC) electrode (Pine-Instruments), which resulted in a 100 µg cm^{-2} catalyst loading. The catalyst ink was prepared by dispersing 5 mg of the catalyst and 28 µL of the 5% Nafion solution (20% of the dry catalyst) in an 875 µL mixture of distilled water and isopropanol solvent (0.7:0.3). Initially, the catalyst was activated by running a CV in N_2-saturated 0.5 M H_2SO_4 electrolyte between 0 and 1.1 V. A CV was then recorded for each of the catalysts in a DME-saturated solution at the same potential range.

For the adsorbed CO (CO_{ads}) stripping experiment, CO gas was bubbled into the electrolyte while holding the catalyst-coated GC working electrode at 0.05 V for 1 min.[45] The excess CO in the solution was then removed by purging N_2 for 20 min. Then the electrode potential was swept between the adsorption potential, 0.05 and 1.2 V at 10 mV s^{-1} to oxidize the CO_{ads} on the catalyst.

Fuel Cell Measurements: For better H^+ conductivity and lower ohmic resistance, a thin membrane (Nafion 211) of 25 µm thickness was used to prepare the catalyst-coated membrane (CCM).[46] The catalyst loading in the anode ($Pt_3Pd_3Sn_2/C$) and cathode (Pt/C) side of the fuel cell was maintained to be 1.55 and 2.20 mg_{PGM} cm^{-2}, respectively. The catalyst ink prepared as above but with only water as a solvent (to prevent shrinkage of the membrane in the presence of isopropanol) was spray coated on the membrane, utilizing an ultrasonic spray-coating system (SimCoat, Sono-Tek) equipped with an ultrasonic generator, a stirring syringe pump, and an ultrasonic spray nozzle. The CCM was sandwiched between a non-teflonized Toray paper (anode side) and teflonized carbon cloth (cathode side), respectively. This assembly was introduced into a fuel cell with a gas flow channel area of 2×2 cm^2.

We followed a similar procedure described in our previous report[3] for operating the DDMEFC. In short, 100% humidified DME and air were supplied to the anode and the cathode at 30 and 400 mL min^{-1}, respectively. The fuel cell temperature was kept at 70 °C. A polarization curve for the DME/air fuel cell was recorded by performing linear sweep voltammetry (LSV) repeatedly in the potential range of open-circuit potential (E_{OC}) of 0.05 V at a scan rate of 5 mV s^{-1} until maximum power density was

achieved. The flow rate of the reactant gases, relative humidity, and *t* temperature was monitored using a humidification system (Fuel Cell Tech, LFHS-C) equipped with analog controllers.

Supporting Information

Supporting Information is available from the Wiley Online Library or from the author.

Conflict of Interest

The authors declare no conflict of interest.

Data Availability Statement

Research data are not shared.

[1] J. T. Müller, P. M. Urban, W. F. Hölderich, K. M. Colbow, J. Zhang, D. P. Wilkinson, *J. Electrochem. Soc.* **2000**, *147*, 4058.

[2] A. Serov, C. Kwak, *Appl. Catal., B* **2009**, *91*, 1.

[3] D. Kashyap, H. Teller, A. Schechter, *ChemElectroChem.* **2019**, *6*, 2407.

[4] Y. Xin, J. G. Liu, Y. Zhou, W. Liu, J. Gao, Y. Xie, Y. Yin, Z. Zou, *J. Power Sources* **2011**, *196*, 1012.

[5] W. Yu, M. D. Porosoff, J. G. Chen, *Chem. Rev.* **2013**, *44*, 5780.

[6] X. Tian, J. Luo, H. Nan, H. Zou, R. Chen, T. Shu, X. Li, Y. Li, H. Song, S. Liao, R. R. Adzic, *J. Am. Chem. Soc.* **2016**, *138*, 1575.

[7] L. M. Salonen, D. Y. Petrovykh, Y. V. Kolen'ko, *Mater. Today Sustainability* **2021**, *11–12*, 100060.

[8] D. Ayodhya, G. Veerabhadram, *Mater. Today Sustainability* **2019**, *5*, 100015.

[9] S. Samad, K. S. Loh, W. Y. Wong, T. K. Lee, J. Sunarso, S. T. Chong, W. R. Wan Daud, *Int. J. Hydrogen Energy* **2018**, *43*, 7823.

[10] J. L. F. Philippe Serp, *Carbon Materials for Catalysis*, John Wiley & Sons, Hoboken, NJ, USA **2009**.

[11] E. J. Oh, R. Hempelmann, V. Nica, I. Radev, H. Natter, *J. Power Sources* **2017**, *341*, 240.

[12] R. Mohan, A. Modak, A. Schechter, *ACS Sustainable Chem. Eng.* **2019**, *7*, 11396.

[13] S. Dou, L. Tao, R. Wang, S. El Hankari, R. Chen, S. Wang, *Adv. Mater.* **2018**, *30*, 1705850.

[14] J. Tang, C. Su, Z. Shao, *Energy Technol.* **2022**, *10*, 2200235.

[15] G. Polymeros, C. Baldizzone, S. Geiger, J. P. Grote, J. Knossalla, S. Mezzavilla, G. P. Keeley, S. Cherevko, A. R. Zeradjanin, F. Schüth, K. J. J. Mayrhofer, *Electrochim. Acta* **2016**, *211*, 744.

[16] C. C. Yang, S. T. Hsu, W. C. Chien, M. Chang Shih, S. J. Chiu, K. T. Lee, C. Li Wang, *Int. J. Hydrogen Energy* **2006**, *31*, 2076.

[17] A. Schechter, H. Teller, D. Kashyap, 16/327,95116/327,951 **2019**.

[18] H. Liu, C. Song, L. Zhang, J. Zhang, H. Wang, D. P. Wilkinson, *J. Power Sources* **2006**, *155*, 95.

[19] G. Wu, Y. S. Chen, B. Q. Xu, *Electrochem. Commun.* **2005**, *7*, 1237.

[20] J. J. Zhang, Z. B. Wang, C. Li, L. Zhao, J. Liu, L. M. Zhang, D. M. Gu, *J. Power Sources* **2015**, *289*, 63.

[21] M. Carmo, A. R. dos Santos, J. G. R. Poco, M. Linardi, *J. Power Sources* **2007**, *173*, 860.

[22] M. Hemmat Esfe, S. Esfandeh, M. Rejvani, *J. Therm. Anal. Calorim.* **2018**, *131*, 1437.

[23] H. Teller, D. Kashyap, S. O. Danino, A. Schechter, *J. Electrochem. Soc.* **2018**, *165*, F1242.

[24] A. S. Meyer, G. H. Ayres, *J. Am. Chem. Soc.* **1955**, *77*, 2671.

[25] A. N. Golikand, M. Asgari, E. Lohrasbi, *Int. J. Hydrogen Energy* **2011**, *36*, 13317.

[26] S. K. Pandey, S. Pandey, V. Parashar, R. S. Yadav, G. K. Mehrotra, A. C. Pandey, *Nanoscale.* **2014**, *6*, 1602.

[27] X. Zhao, T. Gunji, T. Kaneko, S. Takao, T. Sakata, K. Higashi, Y. Yoshida, J. Ge, C. Liu, W. Xing, J. Zhu, M. Xiao, T. Uruga, F. F. Tao, Z. Chen, *J. Mater. Chem. A.* **2020**, *8*, 1368.

[28] B. Murugesan, N. Pandiyan, K. Kasinathan, A. Rajaiah, M. Arumuga, P. Subramanian, J. Sonamuthu, S. Samayanan, V. R. Arumugam, K. Marimuthu, C. Yurong, S. Mahalingam, *Mater. Sci. Eng., C* **2020**, *111*, 110791.

[29] H. Karimi-Maleh, K. Cellat, K. Arıkan, A. Savk, F. Karimi, F. Şen, *Mater. Chem. Phys.* **2020**, *250*, 123042.

[30] Z. Tang, Q. Li, G. Lu, *Carbon* **2007**, *45*, 41.

[31] P. E. Ruiz, B. G. Frederick, W. J. De Sisto, R. N. Austin, L. R. Radovic, K. Leiva, R. García, N. Escalona, M. C. Wheeler, *Catal. Commun.* **2012**, *27*, 44.

[32] L. Stobinski, B. Lesiak, L. Kövér, J. Tóth, S. Biniak, G. Trykowski, J. Judek, *J. Alloys Compd.* **2010**, *501*, 77.

[33] M. Yang, Z. Zhou, *Adv. Sci.* **2017**, *4*, 1600408.

[34] P. Subramanian, A. Cohen, E. Teblum, G. D. Nessim, E. Bormasheko, A. Schechter, *Electrochem. Commun.* **2014**, *49*, 42.

[35] M. Thommes, K. Kaneko, A. V. Neimark, J. P. Olivier, F. Rodriguez-Reinoso, J. Rouquerol, K. S. W. Sing, *Pure Appl. Chem.* **2015**, *87*, 1051.

[36] P. Li, X. Zhang, S. Zhang, *Fuel* **2018**, *224*, 661.

[37] R. Mohan, A. Modak, A. Schechter, *Catal. Sci. Technol.* **2020**, *10*, 1675.

[38] H. Tong, H. L. Li, X. G. Zhang, *Carbon* **2007**, *45*, 2424.

[39] F. P. Lohmann-Richters, B. Abel, Á. Varga, *J. Mater. Chem. A.* **2018**, *6*, 2700.

[40] B. Gavriel, R. Sharabi, L. Elbaz, *ChemSusChem.* **2017**, *10*, 3069.

[41] K. Tonnis, Z. Nan, J. Fang, R. Pavlicek, E. S. DeCastro, A. P. Angelopoulos, *Energy Mater.* **2020**, *3*, 7588.

[42] M. T. García, G. Koper, *Phys. Chem. Chem. Phys.* **2008**, *10*, 3802.

[43] A. Santasalo-Aarnio, M. Borghei, I. V. Anoshkin, A. G. Nasibulin, E. I. Kauppinen, V. Ruiz, T. Kallio, *Int. J. Hydrogen Energy* **2012**, *37*, 3415.

[44] D. Kashyap, H. Teller, A. Schechter, *J. Power Sources* **2018**, *396*, 335.

[45] Z. Li, L. Zhang, X. Huang, L. Ye, S. Lin, *Electrochim. Acta* **2014**, *121*, 215.

[46] J. Ahn, R. Shimizu, K. Miyatake, *J. Mater. Chem. A.* **2018**, *6*, 24625.